Facile preparation of ZnO:g-C$_3$N$_4$ heterostructures and their application in amiloride photodegradation and CO$_2$ photoreduction

Nailma de Jesus Martins [a, b, **], Isabel C.H. Gomes [b], Gelson T.S.T. da Silva [c], Juliana A. Torres [c], Waldir Avansi Jr. [d], Caue Ribeiro [c], Andréa R. Malagutti [e], Henrique A.J.L. Mourão [a, b, *]

[a] Chemistry Postgraduate Program (PPGQ), Federal University of Jequitinhonha and Mucuri Valleys (UFVJM), MGT 367 Highway — Km 583, CEP, 39100-000, Diamantina, MG, Brazil
[b] Institute of Science and Technology (ICT), Federal University of Jequitinhonha and Mucuri Valleys (UFVJM), MGT 367 Highway — Km 583, CEP, 39100-000, Diamantina, MG, Brazil
[c] Nanotechnology National Laboratory for Agriculture (LNNA), Embrapa Instrumentation, 13560-970, São Carlos, SP, Brazil
[d] Department of Physics, Federal University of São Carlos (UFSCar), 13565-905, São Carlos, SP, Brazil
[e] Department of Pharmacy (DEFAR), Federal University of Jequitinhonha and Mucuri Valleys (UFVJM), MGT 367 Highway — Km 583, CEP, 39100-000, Diamantina, MG, Brazil

ARTICLE INFO

ABSTRACT

Semiconductor heterojunctions are interesting strategies for the development of efficient photocatalysts. In this paper we report the synthesis of ZnO:g-C$_3$N$_4$ heterostructures with different percentages of g-C$_3$N$_4$ (15%, 50% and 85%) using an easy and new method: precipitation of ZnO by alkaline solution at room temperature on g-C$_3$N$_4$ surface. The nucleation of ZnO nanoparticles had effective interaction on the g-C$_3$N$_4$ surface, showing good crystallinity and uniformity, which improved the heterostructure stability and the separation of photogenerated charge carriers, consequently increasing the photo-catalytic efficiency for both the degradation of the amiloride (AML) drug and the conversion of CO$_2$ into products such as CO, CH$_4$ and C$_2$H$_4$.

© 2020 Elsevier B.V. All rights reserved.

1. Introduction

Investigations on photocatalytic materials have been carried out to show their importance in different topics, including environmental remediation (i.e. oxidation of organic compounds) and new energy production (i.e. H$_2$ evolution from water and CO$_2$ photoreduction into hydrocarbons) [1,2]. Semiconductors are considered promising materials for such applications since their electronic and structural properties allow the charge transfer and the generation of reactive species responsible for oxidation-reduction reactions in the heterogeneous medium [3]. The conversion efficiency of these processes depends essentially on the light absorption capacity, the generation and separation of photogenerated charge carriers, the adsorption and diffusion of molecules, among others [4,5]. However, a clear understanding of these properties—the oxidative and reductive capacity of semiconductors—and how they influence each process is still a matter of study, essential for the suitable design of future catalysts according to the intended application.

Among several semiconductors, zinc oxide (ZnO) has been widely studied for photocatalysis application due to its several excellent properties [6]. Nevertheless, this oxide is traditionally synthesized by thermal processes, either at high temperatures (above the ambient temperature) or high pressure, in order to obtain the crystalline phase [7—9]. These conditions not only make the synthetic process more complex and costly, but also can

decrease the specific surface area that is essential for catalysis. However, to the best of our knowledge, synthetic methods at ambient temperature for the crystalline ZnO is still little explored in the literature.

The use of ZnO as photocatalyst under prolonged light irradiation can promote its photocorrosion. In addition, for being an amphoteric oxide, ZnO can suffer acid-base chemical reactions in drastic values of pH, either under alkaline or acid conditions [10,11]. These two effects can decrease the effectiveness of the reaction due to ZnO dissolution in the reaction medium by chemical or photocorrosion mechanisms. Therefore, these barriers must be overcome to increase its photocatalytic efficiency. In this light, the coupling of ZnO with other semiconductors appears as a promising alternative [12,13].

The graphitic carbon nitride, g-C_3N_4, is an organic semiconductor widely studied in photocatalytic processes due to its good stability and band gap (2.7 eV) [14–17]. However, in most cases it is coupled to another semiconductor because of its high electron/hole recombination rate, forming heterojunctions. This coupling is responsible for the stabilization of the metal or oxide and the increase in the solar radiation absorption, thus favoring a reaction direction. Although heterojunctions between ZnO and g-C_3N_4 are not new [18–20], there is an increasing necessity for more studies related to methods of impregnation under milder reaction conditions, which can provide good migration of photogenerated charges as a result of the efficient nucleation of ZnO nanoparticles without any loss of surface properties, for instance. Futhermore, the development of simple, efficient and low-cost methods for the synthesis of heterostructures with high stability and photocatalytic properties, especially under visible-light or solar irradiation, can contribute to the consolidation of the use of heterogeneous photocatalysis on a large scale.

Therefore, we describe herein a facile method to synthesize ZnO:g-C_3N_4 heterostructures with different proportions in mass of g-C_3N_4 (15%, 50% and 85%). The synthesized heterostructures were characterized by several techniques and applied for the photodegradation of amiloride and the photoreduction of CO_2.

2. Experimental section

2.1. Materials preparation

The reagents used to prepare the materials were zinc acetate (ISOFAR), melamine (Sigma-Aldrich) and sodium hydroxide (Synth). All reagents were used without further purification.

Firstly, pristine materials were synthesized. The ZnO was prepared by a facile method based on sol-gel hydrolysis as follows: in a typical procedure, a sodium hydroxide solution (1.0 mol L^{-1}) was added to the zinc acetate aqueous solution (0.10 mol L^{-1}) under vigorous stirring until pH = 10, resulting in a white precipitate. After that, the as-formed precipitates were filtrated, washed with deionized water and isopropyl alcohol several times and dried in air at 75 °C. The pristine g-C_3N_4, denoted as CN, was obtained by thermal polycondensation of melamine at 550 °C for 2 h in a conventional furnace in the air atmosphere [21].

The ZnO:g-C_3N_4 heterostructures were synthesized by a simple procedure, as subsequently described. The as-synthesized g-C_3N_4 was dispersed in a zinc acetate aqueous solution at about 0.10 mol L^{-1}, and then a hydroxide sodium solution (1.0 mol L^{-1}) was added under vigorous stirring until pH = 10. Then, the suspensions were also washed and dried at the same conditions of the pure ZnO to produce the powder samples. To obtain heterostructures with different mass contents of ZnO and g-C_3N_4, the synthetic procedure was performed with 15%, 50% and 85% of g-C_3N_4. These samples were referred to as ZnO:CN$_{15\%}$, ZnO:CN$_{50\%}$, and ZnO:CN$_{85\%}$, respectively.

2.2. Materials characterization

X-ray diffraction (XRD) patterns were obtained with an XRD 6000 diffractometer (CuKα radiation) at a scanning speed of 2°/min in the 2θ range from 10° to 90°. The crystallite sizes were calculated using Scherrer's equation [22]. TG-DTA measurements were carried out on a TGA Q500 thermal analyzer (TA Instruments, New Castle, DE) under airflow at a heating rate of 10 °C min^{-1} at temperatures varying from room temperature to 700 °C. Fourier transform infrared (FTIR) spectra were obtained from 400 to 4000 cm^{-1} using a VARIAN 640-IR FT_IR Spectrometer in ATR mode. The images of field emission gun scanning electron microscopy (FEG/SEM) were obtained using a JEOL JSM-6701F microscope. Energy dispersive X-ray spectroscopy (EDS) measurements were performed using an EDS Thermo-Noran equipped with a Si detector attached to the JEOL JEM 2010 microscope. Transmission electron microscopy was performed on a FEI Tecnai G2 F20 microscope. The values of specific surface area (SSA) were estimated according to the Brunauer–Emmett–Teller (BET) method, by using N_2 adsorption data obtained in Micromeritics ASAP-2020 equipment. Diffuse reflectance spectrometry (DRS) analyses were performed with a UV-vis Shimadzu UV-2600 spectrophotometer in the range of 300–700 nm. The band gap energy was estimated by using the Tauc equation from the x-axis intercept of the tangent lines of each curve, as described in a previous study [23].

The photocatalytic performances of the synthesized samples were analyzed in a photoreactor equipped with six fluorescent lamps placed on the top of the reactor with emission in the visible range. This photoreactor was connected to a heat exchanger that maintained the temperature at about 20 °C. Aqueous suspensions were obtained by the dispersion of 10 mg of each photocatalyst in 20 mL of aqueous solutions of the drug amiloride (AML) at 10 mg L^{-1}. Before the photocatalytic test, the suspensions were previously kept in the dark for 12 h to achieve adsorption/desorption equilibrium. The decrease in the AML concentration was analyzed in a Double Beam spectrophotometer (Shimadzu UV 6300 PC equipment) at 285 nm in different periods. All measurements were performed in triplicate. The stability of the synthesized photocatalyst (ZnO:CN$_{50\%}$) was evaluated by performing three recycling experiments with cycles of 260 min each under visible-light irradiation, a total of 780 min (13 h) of catalysis process. The main active species in the photocatalytic degradation process was also investigated. The hydroxyl radical (·OH), hole (h^+) and electron (e^-) were trapped with isopropyl alcohol (20 mmol L^{-1}), potassium bromide (10 mmol L^{-1}) and sodium oxalate (10 mmol L^{-1}), respectively.

The CO_2 photoreduction was performed in a cylindrical steel reactor covered with borosilicate glass with a total volume of 240 mL. Briefly, 0.1 g of catalyst was suspended in 100 mL of distilled water. To remove unwanted gases (O_2 and N_2) inside the reactor, CO_2 was bubbled in the reactor for 20 min in the flow of 20 mL min^{-1}. At the top of the reactor, a 5 W UVC lamp (Philips) with maximum length of 254 nm was inserted, protected by a quartz capsule. The photocatalytic performance of all synthesized materials was monitored for 6 h, and after this period the gaseous and liquid products were collected with a syringe and injected into specific chromatograph equipment. The gaseous products were determined by gas chromatography (Varian, CP-3800). Assays without catalyst were performed to evaluate the photolysis effect and correct the total product formation by photocatalysis.

3. Results and discussion

3.1. Characterization of the synthesized materials

Fig. 1 shows the X-ray diffraction (XRD) patterns of all

synthesized materials: the pristine compounds (ZnO and g-C$_3$N$_4$) and the heterostructures with different mass contents of ZnO and g-C$_3$N$_4$. All diffraction peaks of the ZnO sample are well defined and intense, suggesting that the treatment with sodium hydroxyl at ambient temperature was sufficient to obtain a material with good crystallinity. Such peaks can be indexed to the hexagonal würtzite phase of ZnO [JCPDS nº 36-1451]. The g-C$_3$N$_4$ pattern shows two peaks at 2θ equal to 13° and 27°, which can be attributed to the crystallographic (100) and (002) planes of the graphitic carbon nitride phase [JCPDS nº 87-1526]. These observed peaks are related to an in-plane structural packing motif, such as the hole-to-hole distance of the nitride pores in the crystal and the planar graphitic interlayer distance of g-C$_3$N$_4$, respectively [24]. In the crystallographic pattern of the synthesized compounds with different amounts of ZnO and g-C$_3$N$_4$ we can observe peaks with different intensities, indicating that those related to ZnO become more evident when the oxide amount is increased, as expected.

Table 1 shows the values of the crystallite size of the ZnO phase calculated according to the diffraction peaks of the (100), (002) and (101) planes, and the values of specific surface area (SSA) of the synthesized samples. It seems that ZnO preferably grows in one particular direction since the crystallite sizes perpendicular to the (002) planes were the highest for each sample containing ZnO (ZnO, ZnO:CN$_{15\%}$, ZnO:CN$_{50\%}$, and ZnO:CN$_{85\%}$). In addition, the CN sample and the heterostructures (containing g-C$_3$N$_4$ and ZnO) showed higher SSA than the ZnO.

The synthesized materials were also characterized by TGA, as shown in Fig. 2 a,b. Thermogravimetric analysis was used to estimate the amount of g-C$_3$N$_4$ in the heterostructures since this compound is thermally degraded above 500 °C (see Fig. 2b) under air condition and ZnO is practically stable in this range, losing only 5% of its total mass (see Fig. 2a). The thermogravimetric curves reveal that the pristine ZnO has a small weight loss at low temperatures when heat-treated up to 700 °C, which can be associated with the release of water molecules adsorbed on the material surface [25]. The same contribution was expected in the thermogravimetric results of the synthesized heterostructures, whose curves show that the expected amounts of g-C$_3$N$_4$ were very close to those obtained, demonstrating that the method was efficient to obtain the proportions 85%, 50% and 15%, as seen in Fig. 2a.

On the other hand, in Fig. 2b we can better observe in the derivative weight loss curves that the heterostructures synthesized with g-C$_3$N$_4$ suffered thermal decomposition of g-C$_3$N$_4$ at lower temperatures than the pristine g-C$_3$N$_4$ sample. Our previous studies

Table 1
Crystallite size (D$_{hkl}$) calculated by Scherrer's equation and specific surface area (SSA).

Samples	D$_{hkl}$ (nm)			SSA (m^2 g^{-1})
	(100)	(002)	(101)	
ZnO	39	46	34	6
ZnO:CN$_{15\%}$	35	40	33	15
ZnO:CN$_{50\%}$	38	45	41	11
ZnO:CN$_{85\%}$	33	44	34	21
CN	−	−	−	19

already demonstrated a worse thermal stability of g-C$_3$N$_4$ in the presence of metal oxides or their precursors [21]. This effect is possibly related to the influence of Zn sites on the thermal decomposition of g-C$_3$N$_4$. It is known that metals in thermal reactions with g-C$_3$N$_4$, or even its precursors, can catalyze its decomposition reactions. Even though this effect can be seen in the ZnO:CN$_{15\%}$ and ZnO:CN$_{85\%}$ samples, it is more intense in the ZnO:CN$_{50\%}$, suggesting that its better distribution (i.e. higher ZnO and g-C$_3$N$_4$ contact) could increase the degradation to a maximum; such distribution appears to be lower in the ZnO:CN$_{85\%}$ sample due to its low ZnO content. Additionally, the low amount of g-C$_3$N$_4$ in the ZnO:CN$_{15\%}$ sample might have influenced the reduction of the decomposition temperature.

Fig. 3 shows the FTIR spectra obtained from all the synthesized samples and precursors (melamine and zinc acetate). The spectrum of the pristine ZnO has few peaks, which are attributed to the hydroxyl groups connected to the ZnO surface (3400 cm^{-1}), the Zn-O vibrations at 450 cm^{-1} and the precursor (zinc acetate) residues (1565-1438 cm^{-1}) [25]. However, it is important to note that the quantity of residues is probably the same in all samples, not compromising future performances. From the melamine spectrum, it is possible to observe the presence of vibrational modes attributed to the CN bond (1500-1430 cm^{-1}), the NH bond of the amine group (-NH$_2$) (3500-3000 cm^{-1} and 1650-1600 cm^{-1}) and the deformation of the triazine ring (808 cm^{-1}) [26]. Many of these vibrational modes can be visualized in the g-C$_3$N$_4$ (CN sample) spectrum with the appearance of a broadband centered at approximately 3250 cm^{-1} as a result of the thermal polymerization of triazine rings and the formation of OH groups. The same profile was exhibited for all the synthesized heterostructures, yet with a single difference: the signal at 808 cm^{-1} decreased as the ZnO amount increased, demonstrating that the presence of g-C$_3$N$_4$ or its exposure on the surface of the materials was reduced. Besides this, the intensity of the band in the range between 3600 and 2750 cm^{-1} refers to O-H and N-H vibrations (convoluted peak). This is better visualized in the ZnO:CN$_{85\%}$ sample, where the N-H vibrations are more significant and indicate a slight shift of the sharper peak. Therefore, the higher intensity presented by the ZnO:CN$_{50\%}$ sample can be probably explained by the greater contributions of both shifts, i.e., the O-H vibration is mainly caused by the presence of ZnO, while the N-H vibration mostly appears as a result of the presence of g-C$_3$N$_4$.

Fig. 4 shows the UV-vis spectra obtained from DRS measurements of the synthesized materials. Both pristine g-C$_3$N$_4$ and ZnO have photoabsorption under visible and UV lights, respectively, which is consistent with previous reports [9,27]. On the other hand, all spectra of the synthesized heterostructures showed that the ZnO:g-C$_3$N$_4$ heterostructures have absorption in the visible-light region. In addition, the band gap values decreased to a value similar to that found in the pristine g-C$_3$N$_4$, indicating that the presence of ZnO in the structure contributes poorly to the optical properties of the synthesized heterostructures.

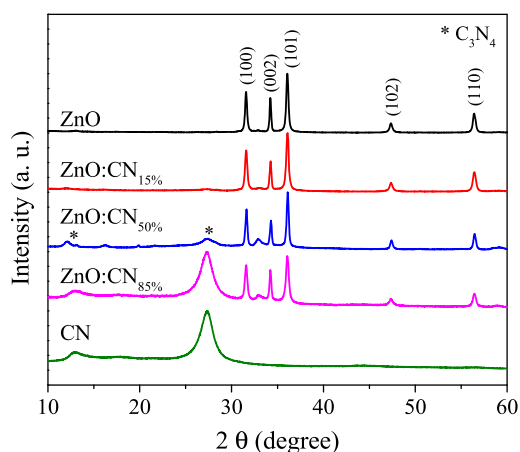The morphology of the synthesized samples can be seen in

Fig. 1. XRD patterns of the synthesized samples. The hkl and symbol (*) identify the main diffraction peaks of the ZnO and g-C$_3$N$_4$ crystalline phases, respectively.
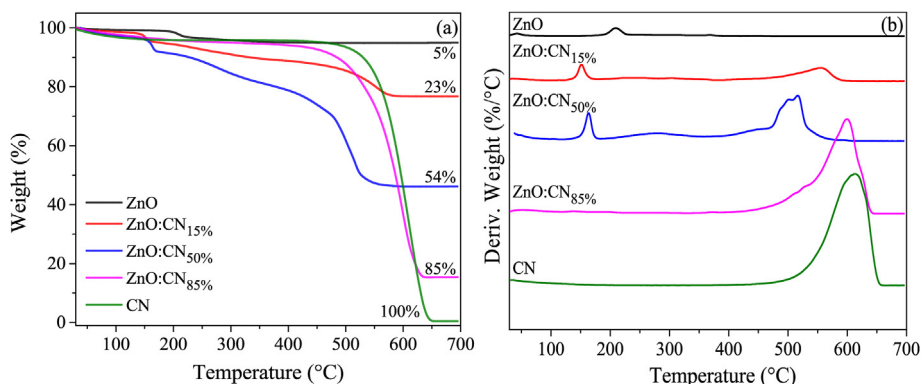
Fig. 2. (a) TG curves showing the mass percent as a function of temperature. The total mass lost is presented at the end of each TG curve. (b) The first derivative of the mass loss curves (%/°C).
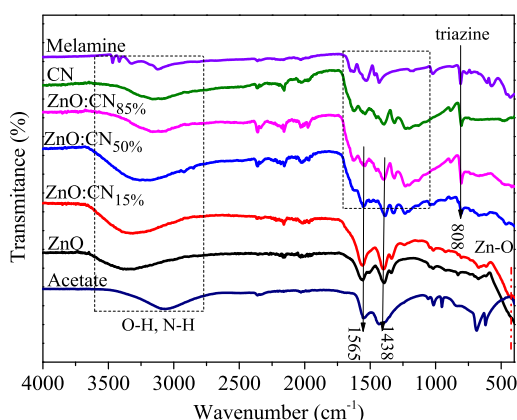

Fig. 3. FTIR spectra obtained from the precursors and all the synthesized samples. More conclusive peaks and bands are highlighted in the spectra.
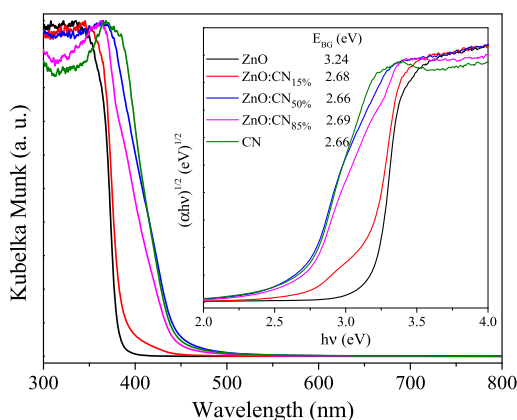

Fig. 4. UV-vis diffuse reflectance spectra and Tauc plot (in the inset) for indirectly allowed transition obtained from UV-vis diffuse reflectance spectra data. The values of band gap (E_{BG}) are also shown in the inset.

Fig. 5. The SEM micrograph of the pristine g-C_3N_4 (Fig. 5a) demonstrates that the synthesized powder has the typical lamellar agglomerate morphology [21]. The SEM image of the ZnO sample (Fig. 5b) shows irregular rod-like particles with micrometric lengths and hexagonal base of approximately 100 nm, as seen in the inset of Fig. 5b. In contrast, the representative image of the ZnO:CN$_{50\%}$ sample (Fig. 5c) reveals the existence of irregular rod-

like particles and lamellar materials, indicating the presence of ZnO and g-C_3N_4, respectively. Besides that, the inset of Fig. 5c also suggests that the synthesis method effectively caused good nucleation of ZnO particles on the g-C_3N_4 surface, producing an intimate contact between them, consequently resulting in the formation of heterojunctions between the semiconductors.

A representative TEM image of the ZnO:CN$_{50\%}$ sample (Fig. 5d) reveals the existence of two distinct morphologies: lamellar and spherical/hexagonal nanomaterials. The HRTEM image (Fig. 5e) confirms that the spherical/hexagonal nanostructures are related to the ZnO hexagonal wurtzite since it showed an interlayer distance of 0.25 nm, which can be assigned to (101) crystalline plane of this phase. In addition, Fig. S1 brings a representative EDS mapping analysis (b-d) from the region shown in Fig. S1a of the representative ZnO:CN$_{50\%}$ sample, which confirms the presence and coexistence of elements related to ZnO and g-C3N4, such as C, N, Zn and O. A good homogeneity in the distribution of g-C3N4 and ZnO particles can also be observed.

Therefore, according to our SEM, TEM and EDS results, it was possible to conclude that the ZnO rods consist of agglomerates formed by a large number of smaller ZnO nanoparticles sized between 5 and 20 nm. This behavior was already observed by different materials, such as BiVO$_4$, where a larger particle is composed of smaller particles [28]. We could also infer that the ZnO particles are attached to the g-C_3N_4, thus forming the ZnO:C_3N_4 heterostructures.

3.2. Photocatalytic tests

3.2.1. Photo-oxidation properties

Fig. 6 displays the photodegradation curves of the amiloride (AML) drug under visible light. In addition, Table S1 shows the reaction rate constants (kp) that were calculated using a pseudo-zero-order model [29]. In the presence of the synthesized materials, there was an improvement in the degradation of the AML solution compared to the photolysis process (negligible degradation), demonstrating that the such materials are promising catalysts in the oxidation of this drug. Also, the pristine semiconductors (ZnO and g-C_3N_4) showed poor activity compared to all synthesized heterostructures, degrading about 15% and 22% of AML, respectively. The low photocatalytic activity exhibited by these pristine materials was already expected as the tests were carried out under visible-light irradiation, and this spectral range is not sufficient to activate ZnO. It is worth mentioning that the g-C_3N_4 is known to have a high rate of recombination of photogenerated charge carriers [30]. Thus, the presence of g-C_3N_4 was crucial for the photoactivation under visible-light irradiation, and the coupling of ZnO
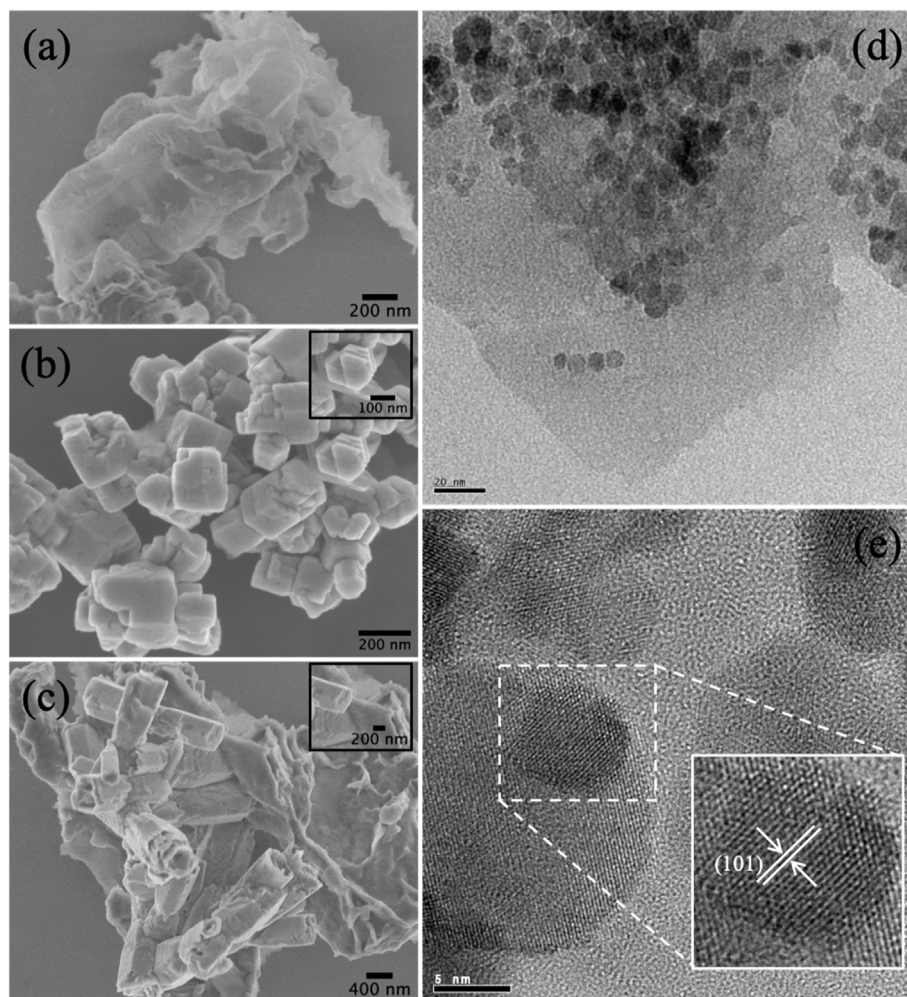
Fig. 5. FEG/SEM images of the synthesized samples: a) CN; b) ZnO; c) ZnO:CN$_{50\%}$. The expanded views of 'b' and 'c' reveal rod-like ZnO particles and both materials (ZnO and g-C$_3$N$_4$) together, respectively. TEM (d) and HRTEM (e) images of the ZnO:CN$_{50\%}$ sample. The inset in (e): an expanded view of the HRTEM image for a representative ZnO nanoparticle.
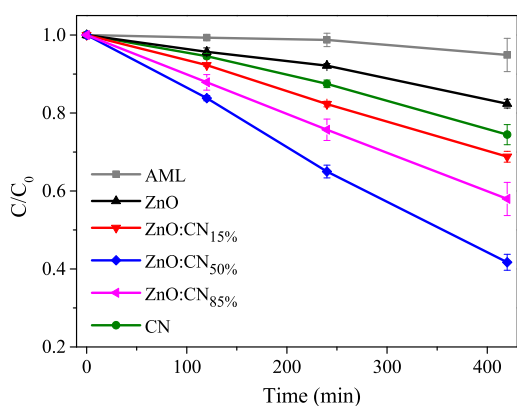

Fig. 6. Photodegradation curves of the amiloride (AML) comparing the direct photolysis with its degradation in the presence of the synthesized photocatalysts under visible-light irradiation.

with g-C$_3$N$_4$ was fundamental to improve the photocatalytic efficiency of the prepared heterostructures compared to the pristine materials. In addition, the ZnO:CN$_{50\%}$ sample had the best photocatalytic performance (about 53% of degradation), according to Fig. 6. In this way, these results suggest the formation of heterojunctions between the ZnO and g-C$_3$N$_4$ phases, which induces an increase in the separation of the photogenerated charges through charge transfer from g-C$_3$N$_4$ to ZnO, since the association of these phases showed a positive synergistic effect for the photodegradation process. In the intermediate proportion of each heterostructure component, i.e. 50% (ZnO:CN$_{50\%}$), the number of heterojunctions is probably greater than in other samples, as the components (g-C$_3$N$_4$ and ZnO) tend to be more dispersed and less segregated.

For being a fundamental characteristic of a good catalyst, especially in large-scale processes, the stability of the synthesized photocatalyst with the best performance for AML degradation under visible light, ZnO:CN$_{50\%}$, was analyzed. In Fig. 7, we can see no significant deactivation of the analyzed photocatalyst after successive re-uses, demonstrating that the studied systems (ZnO:CN heterostructures) can be employed to stabilize ZnO in photocatalytic processes. This may be associated with the fact that apparently there was neither photo nor chemical corrosion with oxide, as the materials exhibited good photostability and good performance to degrade amiloride under visible-light irradiation even after 13 h of use.

To investigate the active species in the AML photodegradation driven by the ZnO:CN$_{50\%}$ heterostructure under visible light, some scavengers were added to the reaction, e.g., isopropyl alcohol
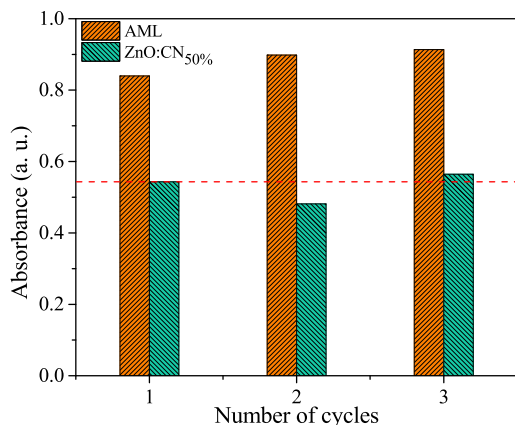
Fig. 7. Stability of the ZnO:CN$_{50\%}$ (green bar) photocatalyst during three cycles of AML photodegradation. AML direct photolysis was also presented for comparison. (For interpretation of the references to colour in this figure legend, the reader is referred to the Web version of this article.)

(scavenger for the hydroxyl radical, ·OH), potassium bromide (scavenger for the electron e^-) and sodium oxalate (scavenger for the hole h^+) (Fig. 8). In this experiment, we observed that the sequestering agents added to the reactions fulfilled their role and decreased the AML degradation rate caused by the synthesized photocatalyst. With that in mind, it was demonstrated that all the photogenerated species participate in the AML degradation mechanism.

Based on our results and several important studies regarding heterogeneous photocatalysis [18,20,31,32], we proposed a hypothetical mechanism (Fig. 9a) to illustrate the formation and migration of charges as well as the oxidation and reduction processes in the valence (VB) and conduction (CB) bands, respectively. First, due to the presence of g-C$_3$N$_4$ in a conventional type-II heterostructure, the heterostructures are photoactivated under visible-light irradiation—although they could also be activated by solar radiation. In this case, the ZnO is not photoactive because of its high value of band gap, making unfeasible the possibility of direct Z-scheme [33–35]. Second, there is the formation of oxidizing charges in the VB (h^+) and reducers in the CB (e^-) in the photo-actived g-C$_3$N$_4$. The VB participates in the oxidation reactions, and the photogenerated electrons are first migrated to the CB of g-C$_3$N$_4$, and then transferred to the CB of ZnO. This charge transfer process is essential to decrease the charge carrier recombination and consequently increase the photocatalytic activity; this is the principle of a conventional type-II heterostructure. The charge generated (h^+) in the VB can act as a direct oxidizing agent and degrade
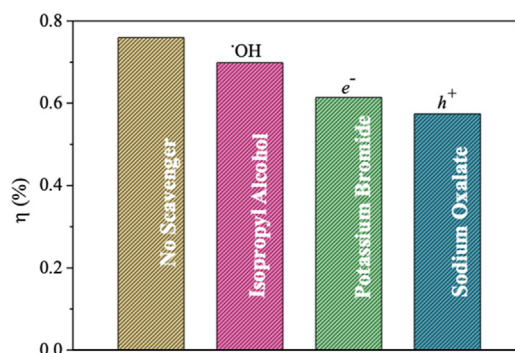

Fig. 8. The effects of scavengers on the efficiency of AML degradation with the ZnO:CN$_{50\%}$ photocatalyst under visible-light irradiation.

the organic molecule, or oxidize water, generating hydroxyl radicals, species with a high oxidizing capacity. In other words, the degradation can occur indirectly by the oxidation of AML molecules through their interaction with the formed species (i.e. ·OH), or directly by their interaction with the generated charges, especially the direct oxidation of AML molecules by the holes originating from the BV of g-C$_3$N$_4$. This direct oxidation by holes can begin with the formation of AML radicals (·AML$^+$), responsible for subsequent reactions of the AML degradation. According to Fig. 8, the holes (h^+) contribute to the degradation of AML more than other species since they can participate in the formation of both ·OH and ·AML$^+$. On the other hand, the electrons transferred to the CB of ZnO can reduce the molecular oxygen, forming the superoxide radical (·O$_2^-$), a species with a high oxidizing capacity that later oxidizes the organic molecules, or oxidizes water, also generating hydroxyl radicals.

3.2.2. CO$_2$ photoreduction properties

The catalytic capacity of these materials (except the pristine ZnO) was also monitored with respect to the reduction of CO$_2$, a molecule responsible for several climatic changes. Fig. 10 shows the results of the photocatalytic reduction of CO$_2$ into CO, CH$_4$ and C$_2$H$_4$. The pristine ZnO did not have satisfactory results in relation to CO$_2$ conversion, because under experimental conditions this oxide is completely dissolved, as expected. It occurs due to acidic species (HCO$_3^-$ and H$_2$CO$_3$) formed when CO$_2$ is dissolved in water, leading to ZnO instability, especially under irradiation. This effect was not observed in the experiments with other prepared samples (g-C$_3$N$_4$ and heterostructures), confirming the results observed in Fig. 7, where the use of g-C$_3$N$_4$ not only improved the activity of the synthesized materials, but also increased their photochemical stability in photocatalytic processes.

From Fig. 10, it is possible to observe that the pristine g-C$_3$N$_4$ showed a moderate selectivity for CO formation after 6 h of reaction despite the fact that the observed CO production was low (0.56 μmol/g) compared to the other samples, demonstrating that the formation of heterojunctions with ZnO makes the materials more efficient due to the improved separation of photogenerated charge carriers [36]. It can also be noted that the ZnO:CN$_{85\%}$ sample (1.64 μmol/g) exhibited a greater activity than the pristine g-C$_3$N$_4$, indicating that there is a tendency towards the improvement of such activity as a consequence of the presence of ZnO. This influence can be better observed in the ZnO:CN$_{50\%}$ sample, whose production was 12.73 μmol/g. However, when more ZnO (ZnO:CN$_{15\%}$) was added we could notice a drop in the production of CO (1.37 μmol/g), suggesting that although ZnO is fundamental for the catalytic activity of the material an excessive amount can come to pile up the ZnO rods, agglomerating all of them in the same region. As a result, the interaction with g-C$_3$N$_4$ was reduced, causing a low sharing of photogenerated charges, consequently decreasing the lifetime of the electron/hole pairs. This decrease in the interaction with g-C$_3$N$_4$ can also lead to undesirable photo or chemical corrosion since the g-C$_3$N$_4$ surface used as a stabilizing agent will not be available for coupling.

Furthermore, the synthesized heterostructures showed good catalytic performance for the conversion of CO$_2$ into other products, such as CH$_4$ and C$_2$H$_4$, as it can be seen in Fig. 10. The results demonstrate that the synthesized heterostructures (ZnO:CN$_{15\%}$, ZnO:CN$_{50\%}$, and ZnO:CN$_{85\%}$) produced low amounts of C$_2$H$_4$, which were close to the detection limit of the equipment, making it difficult to analyze the results. However, it is possible to observe a trend of the ZnO:CN$_{50\%}$ sample (0.49 μmol/g) to be more effective than other samples (0.15 and 0.16 μmol/g for ZnO:CN$_{15\%}$ and ZnO:CN$_{85\%}$, respectively). The C$_2$H$_4$ production involves high energy to promote -CH$_2$ dimerization, low stability of the formed
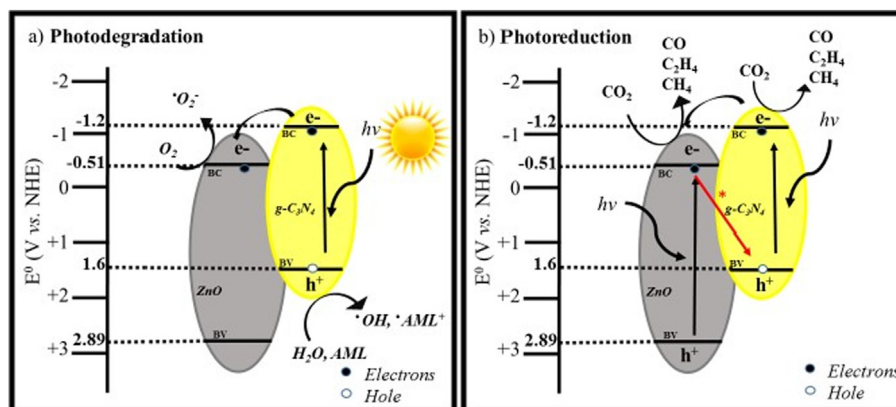
Fig. 9. Schematic illustration of a) AML photodegradation and b) CO_2 photoreduction using the synthesized heterostructures. *Direct Z-scheme: possible recombination between e^- of the ZnO with h^+ of the g-C_3N_4.
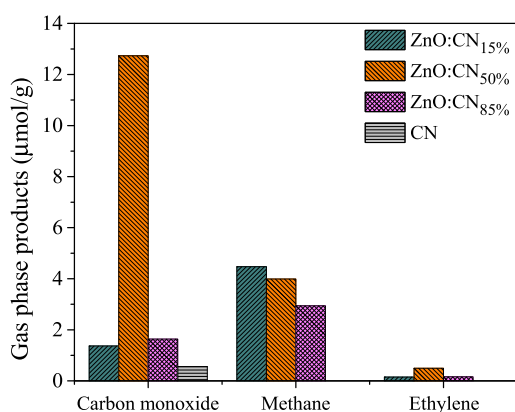

Fig. 10. Catalytic CO_2 photoreduction products after 6 h of reaction.

intermediates and successive number of steps that the specimens must undergo to form such product [37]. On the other hand, the CH_4 production showed that the low exposure of g-C_3N_4 did not affect the performance of the ZnO:$CN_{15\%}$ heterostructures (4.47 μmol/g) compared to 3.99 and 2.94 μmol/g for ZnO:$CN_{50\%}$ and ZnO:$CN_{85\%}$, respectively, indicating a moderate selectivity of the sample to ZnO catalytic sites.

Therefore, the good photocatalytic performance of the analyzed materials during the CO_2 conversion can be mainly attributed to: (i) the stability of ZnO promoted by the coupling with the g-C_3N_4 surface; and (ii) the formation of type-II heterostructures that favored the migration of the photogenerated charges and increased the reduction potential of the photocatalyst. It is important to highlight that the direct Z-scheme would be also possible considering that the CO_2 photoreduction tests were carried out under UV irradiation, which enables the photoactivation of both semiconductors (ZnO and g-C_3N_4) [33–35]. This effect could positively influence the reduction potential of the heterostructure since the CO_2 reduction could occur in the CB of the g-C_3N_4 (Fig. 9b), which presents higher reduction potential than the BC of the ZnO.

4. Conclusions

Highly crystalline ZnO nanoparticles and ZnO:g-C_3N_4 heterostructures were successfully prepared by a facile method at controlled pH. The synthesized heterostructures showed distinct properties, such as visible light photoactivation, chemical and photo stabilities, better separation of the photogenerated electron-hole pairs, among others. In general, the ZnO:$CN_{50\%}$ sample exhibited outstanding performance for both AML photodegradation and CO_2 reduction, especially with regard to CO production, which was attributed to synergetic effects associated with the presence of heterojunctions between the two phases: ZnO and g-C_3N_4.

CRediT authorship contribution statement

Nailma de Jesus Martins: Conceptualization, Methodology, Investigation, Writing - original draft. **Isabel C.H. Gomes:** Methodology, Investigation. **Gelson T.S.T. da Silva:** Conceptualization, Methodology, Investigation, Writing - original draft. **Juliana A. Torres:** Conceptualization, Methodology, Investigation, Writing - original draft. **Waldir Avansi:** Conceptualization, Methodology, Investigation, Resources, Writing - original draft. **Caue Ribeiro:** Conceptualization, Supervision, Resources, Funding acquisition, Writing - original draft. **Andréa R. Malagutti:** Conceptualization, Supervision, Resources, Writing - original draft. **Henrique A.J.L. Mourão:** Conceptualization, Methodology, Resources, Writing - original draft, Supervision, Funding acquisition, Project administration.

Declaration of competing interest

The authors declare that they have no known competing financial interests or personal relationships that could have appeared to influence the work reported in this paper.

Acknowledgments

Appendix A. Supplementary data

Supplementary data to this article can be found online at https://doi.org/10.1016/j.jallcom.2020.156798.

References

[1] V.R. de Mendonça, O.F. Lopes, A.E. Nogueira, G.T.S.T. da Silva, C. Ribeiro, Challenges of synthesis and environmental applications of metal-free nano-heterojunctions, in: Inamuddin, G. Sharma, A. Kumar, E. Lichtfouse, A.M. Asiri (Eds.), Nanophotocatalysis and Environmental Applications, Springer International Publishing, Cham, 2019, pp. 107−138, https://doi.org/10.1007/978-3-030-10609-6_4.

[2] S. Wang, Y. Wang, S. Zang, X.W. David Lou, Hierarchical hollow heterostructures for photocatalytic CO2 reduction and water splitting, Small Methods 4 (2020), 1900586, https://doi.org/10.1002/smtd.201900586.

[3] R. Bueno, O. Lopes, K. Carvalho, C. Ribeiro, H. Mourão, Heterostructured semiconductors: an approach about the main challenges for obtaining and application on environmental and energy photochemical processes, Química Nova, 2019, https://doi.org/10.21577/0100-4042.20170372.

[4] C. Xu, P. Ravi Anusuyadevi, C. Aymonier, R. Luque, S. Marre, Nanostructured materials for photocatalysis, Chem. Soc. Rev. 48 (2019) 3868−3902, https://doi.org/10.1039/C9CS00102F.

[5] M. Xiao, Z. Wang, M. Lyu, B. Luo, S. Wang, G. Liu, H. Cheng, L. Wang, Hollow nanostructures for photocatalysis: advantages and challenges, Adv. Mater. 31 (2019), 1801369, https://doi.org/10.1002/adma.201801369.

[6] S.B.A. Hamid, S.J. Teh, C.W. Lai, Photocatalytic water oxidation on ZnO: a Review, Catalysts 7 (2017) 93, https://doi.org/10.3390/catal7030093.

[7] G. Byzynski, A.P. Pereira, D.P. Volanti, C. Ribeiro, E. Longo, High-performance ultraviolet-visible driven ZnO morphologies photocatalyst obtained by microwave-assisted hydrothermal method, J. Photochem. Photobiol. Chem. 353 (2018) 358−367, https://doi.org/10.1016/j.jphotochem.2017.11.032.

[8] J. Wojnarowicz, T. Chudoba, I. Koltsov, S. Gierlotka, S. Dworakowska, W. Lojkowski, Size control mechanism of ZnO nanoparticles obtained in microwave solvothermal synthesis, Nanotechnology 29 (2018), 065601, https://doi.org/10.1088/1361-6528/aaa0ef.

[9] G.T.S.T. da Silva, K.T.G. Carvalho, O.F. Lopes, E.S. Gomes, A.R. Malagutti, V.R. Mastelaro, C. Ribeiro, H.A.J.L. Mourão, Synthesis of ZnO nanoparticles assisted by N sources and their application in the photodegradation of organic contaminants, ChemCatChem 9 (2017) 3795−3804, https://doi.org/10.1002/cctc.201700756.

[10] L. Zhang, H. Cheng, R. Zong, Y. Zhu, Photocorrosion suppression of ZnO nanoparticles via hybridization with graphite-like carbon and enhanced photocatalytic activity, J. Phys. Chem. C 113 (2009) 2368−2374, https://doi.org/10.1021/jp807778r.

[11] A. Degen, M. Kosec, Effect of pH and impurities on the surface charge of zinc oxide in aqueous solution, J. Eur. Ceram. Soc. (2000) 7.

[12] S. Kumar, A. Kumar, A. Kumar, V. Krishnan, Nanoscale zinc oxide based heterojunctions as visible light active photocatalysts for hydrogen energy and environmental remediation, Catal. Rev. (2019) 1−60, https://doi.org/10.1080/01614940.2019.1684649.

[13] C.B. Ong, L.Y. Ng, A.W. Mohammad, A review of ZnO nanoparticles as solar photocatalysts: synthesis, mechanisms and applications, Renew. Sustain. Energy Rev. 81 (2018) 536−551, https://doi.org/10.1016/j.rser.2017.08.020.

[14] J. Li, C. Tian, H. Zhao, J. Mei, J. Zhang, S. Yang, Controllable fabrication of a red phosphorus modified g-C3N4 photocatalyst with strong interfacial binding for the efficient removal of organic pollutants, J. Alloys Compd. 810 (2019), 151885, https://doi.org/10.1016/j.jallcom.2019.151885.

[15] H. Tang, R. Wang, C. Zhao, Z. Chen, X. Yang, D. Bukhvalov, Z. Lin, Q. Liu, Oxamide-modified g-C3N4 nanostructures: tailoring surface topography for high-performance visible light photocatalysis, Chem. Eng. J. 374 (2019) 1064−1075, https://doi.org/10.1016/j.cej.2019.06.029.

[16] C. Zhao, Z. Chen, J. Xu, Q. Liu, H. Xu, H. Tang, G. Li, Y. Jiang, F. Qu, Z. Lin, X. Yang, Probing supramolecular assembly and charge carrier dynamics toward enhanced photocatalytic hydrogen evolution in 2D graphitic carbon nitride nanosheets, Appl. Catal. B Environ. 256 (2019), 117867, https://doi.org/10.1016/j.apcatb.2019.117867.

[17] G. Mamba, A.K. Mishra, Graphitic carbon nitride (g-C 3 N 4) nanocomposites: a new and exciting generation of visible light driven photocatalysts for environmental pollution remediation, Appl. Catal. B Environ. 198 (2016) 347−377, https://doi.org/10.1016/j.apcatb.2016.05.052.

[18] H. Jung, T.-T. Pham, E.W. Shin, Effect of g-C3N4 precursors on the morphological structures of g-C3N4/ZnO composite photocatalysts, J. Alloys Compd. 788 (2019) 1084−1092, https://doi.org/10.1016/j.jallcom.2019.03.006.

[19] M. Sun, Z. Chen, X. Jiang, C. Feng, R. Zeng, Optimized preparation of Co-Pi decorated g-C3N4@ZnO shell-core nanorod array for its improved photoelectrochemical performance and stability, J. Alloys Compd. 780 (2019) 540−551, https://doi.org/10.1016/j.jallcom.2018.12.019.

[20] Y. He, Y. Wang, L. Zhang, B. Teng, M. Fan, High-efficiency conversion of CO2 to fuel over ZnO/g-C3N4 photocatalyst, Appl. Catal. B Environ. 168−169 (2015) 1−8, https://doi.org/10.1016/j.apcatb.2014.12.017.

[21] M.A. Ferreira, G.T.S.T. da Silva, O.F. Lopes, V.R. Mastelaro, C. Ribeiro, M.J.M. Pires, A.R. Malagutti, W. Avansi, H.A.J.L. Mourão, Fabrication of SrTiO3/g-C3N4 heterostructures for visible light-induced photocatalysis, Mater. Sci. Semicond. Process. 108 (2020), 104887, https://doi.org/10.1016/j.mssp.2019.104887.

[22] P. Bindu, S. Thomas, Estimation of lattice strain in ZnO nanoparticles: X-ray peak profile analysis, J. Theor. Appl. Phys. 8 (2014) 123−134, https://doi.org/10.1007/s40094-014-0141-9.

[23] A. Murphy, Band-gap determination from diffuse reflectance measurements of semiconductor films, and application to photoelectrochemical water-splitting, Sol. Energy Mater. Sol. Cell. 91 (2007) 1326−1337, https://doi.org/10.1016/j.solmat.2007.05.005.

[24] I.F. Teixeira, E.C.M. Barbosa, S.C.E. Tsang, P.H.C. Camargo, Carbon nitrides and metal nanoparticles: from controlled synthesis to design principles for improved photocatalysis, Chem. Soc. Rev. 47 (2018) 7783−7817, https://doi.org/10.1039/C8CS00479J.

[25] T.R. Giraldi, G.V.F. Santos, V.R. Mendonça, C. Ribeiro, I.T. Weber, Annealing effects on the photocatalytic activity of ZnO nanoparticles, J. Nanosci. Nanotechnol. 11 (2011) 3635−3640, https://doi.org/10.1166/jnn.2011.3801.

[26] N.E. Mircescu, M. Oltean, V. Chiş, N. Leopold, FTIR, FT-Raman, SERS and DFT study on melamine, Vib. Spectrosc. 62 (2012) 165−171, https://doi.org/10.1016/j.vibspec.2012.04.008.

[27] S.C. Yan, Z.S. Li, Z.G. Zou, Photodegradation performance of g-C3N4 fabricated by directly heating melamine, Langmuir 25 (2009) 10397−10401, https://doi.org/10.1021/la900923z.

[28] O.F. Lopes, K.T.G. Carvalho, A.E. Nogueira, W. Avansi, C. Ribeiro, Controlled synthesis of BiVO4 photocatalysts: evidence of the role of heterojunctions in their catalytic performance driven by visible-light, Appl. Catal. B Environ. 188 (2016) 87−97, https://doi.org/10.1016/j.apcatb.2016.01.065.

[29] H.A.J.L. Mourão, C. Ribeiro, TiO2 and SnO2 magnetic nanocomposites: influence of semiconductors and synthetic methods on photoactivity, J. Nanosci. Nanotechnol. 11 (2011) 7876−7883, https://doi.org/10.1166/jnn.2011.4712.

[30] P. Niu, L. Zhang, G. Liu, H.-M. Cheng, Graphene-like carbon nitride nanosheets for improved photocatalytic activities, Adv. Funct. Mater. 22 (2012) 4763−4770, https://doi.org/10.1002/adfm.201200922.

[31] O. Legrini, E. Oliveros, A.M. Braun, Photochemical processes for water treatment, Chem. Rev. 93 (1993) 671−698, https://doi.org/10.1021/cr00018a003.

[32] M.R. Hoffmann, S.T. Martin, Wonyong Choi, D.W. Bahnemann, Environmental applications of semiconductor photocatalysis, Chem. Rev. 95 (1995) 69−96, https://doi.org/10.1021/cr00033a004.

[33] G. Liu, L. Wang, H.G. Yang, H.-M. Cheng, G.Q. Max Lu, Titania-based photocatalysts—crystal growth, doping and heterostructuring, J. Mater. Chem. 20 (2010) 831−843, https://doi.org/10.1039/B909930A.

[34] C. Zhao, L. Tian, Z. Zou, Z. Chen, H. Tang, Q. Liu, Z. Lin, X. Yang, Revealing and accelerating interfacial charge carrier dynamics in Z-scheme heterojunctions for highly efficient photocatalytic oxygen evolution, Appl. Catal. B Environ. 268 (2020), 118445, https://doi.org/10.1016/j.apcatb.2019.118445.

[35] X. Yang, L. Tian, X. Zhao, H. Tang, Q. Liu, G. Li, Interfacial optimization of g-C3N4-based Z-scheme heterojunction toward synergistic enhancement of solar-driven photocatalytic oxygen evolution, Appl. Catal. B Environ. 244 (2019) 240−249, https://doi.org/10.1016/j.apcatb.2018.11.056.

[36] W. Yu, D. Xu, T. Peng, Enhanced photocatalytic activity of g-C3N4 for selective CO2 reduction to CH3OH via facile coupling of ZnO: a direct Z-scheme mechanism, J. Mater. Chem. A. 3 (2015) 19936−19947, https://doi.org/10.1039/C5TA05503B.

[37] D. Gao, R.M. Arán-Ais, H.S. Jeon, B. Roldan Cuenya, Rational catalyst and electrolyte design for CO2 electroreduction towards multicarbon products, Nat. Catal. 2 (2019) 198−210, https://doi.org/10.1038/s41929-019-0235-5.